On-Orbit Geometric Calibration of the HJ-2 A/B Satellites' Infrared Sensors

Hao Zhang [1], Wei Qin [1], Kaixin Wang [2], Qianying Wang [2], Pengjie Tao [1, 3, *]

[1] School of Remote Sensing and Information Engineering, Wuhan University, Wuhan 430079, China - zhanghowe@whu.edu.cn, wei-qin@whu.edu.cn, pjtao@whu.edu.cn
[2] Institution of Remote Sensing Satellite, Chinese Academy of Space Technology, Beijing 100094, China - 784530474@qq.com, bitwqy@163.com
[3] Hubei Luojia Laboratory, Wuhan 430079, China

Keywords: Camera calibration, Infrared sensors, Whisk-broom camera, Multi-focal-plane-array, HJ-2 A/B satellites.

Abstract

With the advancement of China's satellite technology, the HuanJingJianZai-2 A/B (HJ-2 A/B) satellites, equipped with whisk-broom infrared sensors, represent a significant leap forward in environmental monitoring and Earth observation capabilities. This technological leap, however, introduces new challenges in calibration. The unique structure of the HJ-2 A/B infrared spectroradiometer (IRS) necessitates innovative calibration techniques, as traditional methods primarily focused on exterior orientation parameters (EOPs) and often overlooked the importance of interior orientation accuracy, which is essential for accurate multispectral band registration and color rendering. Addressing this gap, we introduce an innovative multi-focal-plane-array joint calibration method specifically designed for whisk-broom cameras. Our method involves selecting a master band from each focal plane array for accurate focal length calibration and deriving ground control points from image matching and altitude interpolation for comprehensive bundle adjustment. This adjustment refines EOPs and interior orientation parameters (IOPs), ensuring globally optimal EOPs and enhanced IOPs calibration stability. The application of our method to the HJ-2 A/B IRS yielded substantial improvements in georeferencing and band registration accuracies, surpassing traditional methods. This paper details the multi-focal-plane-array joint calibration method, describes the IRS and experimental setup, presents the experimental results, and concludes with the implications and potential applications of our findings.

1. Introduction

Infrared sensors, crucial for tasks such as vegetation analysis and smoke detection (Corsi, 2010; Liu et al., 2021), are increasingly adopting whisk-broom mode for broader data collection, as seen in MODIS, AVHRR, and MERSI-II (Fowler et al., 2014). The HuanJingJianZai-2 A/B (HJ-2 A/B) satellites, pivotal elements in China's remote sensing endeavors, represent a significant leap in high-resolution (HR) environmental observation technology. These two satellites, equipped with advanced whisk-broom infrared spectroradiometers (IRS), were specifically launched to meet the complex demands of Earth's environmental monitoring and observation. The focus of the HJ-2 A/B is primarily on thermal infrared imaging, a crucial aspect for applications ranging from land resource management to disaster management. The unique structure of the IRS on these satellites presents specialized calibration and geometric correction challenges. To obtain better inversion results in terms of the position and area of interest through the improvement of georeferencing accuracy, the on-orbit calibration of spaceborne sensors is necessary, which includes exterior orientation parameters (EOPs) and interior orientation parameters (IOPs) calibration (Garcia et al., 2020; Tao et al., 2014; Zhang et al., 2013). Moreover, the dynamic nature of whisk-broom sensors, with their rotating mirrors, introduces more complex calibration challenges than push-broom sensors (Li, 2021; Sheng et al., 2018).

To achieve stable and high georeferencing accuracy, it is essential to analyze and compensate the systematic errors of whisk-broom sensors through calibration (Hugenholtz et al., 2016). In the early era of whisk-broom sensor georeferencing development, much effort was devoted to reducing errors caused by inaccurate measurement of ephemeris and attitude for satellite navigation (Ye et al., 2017; Toutin, 2004). Benefitting from improved ephemeris accuracy (Caporali et al., 2021), compensation for attitude can achieve sub-pixel georeferencing accuracy, as reported in studies of AVHRR and microwave radiation imager (Fang et al., 2021). However, these studies mainly aimed at improving the exterior orientation accuracy. Attention should also be paid to the interior orientation accuracy to achieve better multispectral band registration performance, important for good color rendering and sharp area estimation of ground objects. Consequently, many studies have been conducted to compensate for the systematic errors within dynamic sensors (Pan et al., 2022a; Schorlemer et al., 2021). The study on the YaoGan-14's thermal-infrared sensor involved calibrating temporal system parameters and whisk-broom angle parameters, a process that successfully achieved plane positioning accuracy at the sub-pixel level (Sheng et al., 2018). Furthermore, systematic errors in MERSI-II, such as pitch angle errors of K-mirrors and principal distance error, were significantly reduced, achieving a root mean square error (RMSE) of 0.4 pixels in nadir image (Pan et al., 2022b). To calibrate different band arrays, these studies adopted a band-to-band registration method (Tilton et al., 2019). Specifically, a master band, whose wavelength is close to the visible spectral band, is generally first selected to match reliable ground control points (GCPs) from reference digital orthophoto maps (DOMs) and be calibrated after optimization the attitudes and scanning angles by bundle adjustment (Cao et al., 2019; Tong et al., 2019), then the other slave bands are calibrated based on the EOPs of the master band. However, this method is not suitable for those whisk-broom sensors with multiple focal plane arrays (FPAs) since the master band does not share the same focal length with the slave bands on different FPAs. Besides, the corresponding ground objects on different bands are observed at different times,

---

which means the master and slave bands suffer different exterior orientation errors during the same exposure period (Liu et al., 2012). Thus, the calibration strategy using one master band for bundle adjustment is not stable because the difference between focal lengths of different FPAs is ignored and the EOPs may not be global optimal due to the fact that the slave bands are not participated in the bundle adjustment.

To address the above issue, we propose a multi-focal-plane-array joint calibration method for whisk-broom sensors. First, for each FPA, a master band is selected to calibrate the focal length. Secondly, GCPs are obtained based on matching these master band images with the reference DOMs and interpolating their altitudes from reference digital elevation models (DEMs). Thirdly, GCPs on all the master band images participate in bundle adjustment for refining the EOPs and IOPs of master bands. Finally, the IOPs of the slave bands are calibrated based on the global optimal EOPs and their corresponding focal lengths. Our method's major innovation, compared to methods selecting a single master band for all FPAs, lies in achieving globally optimal EOPs for different FPAs and accurately calibrating their focal lengths, resulting in more stable IOPs.

The IRS adopted in HJ-2 A/B was successfully calibrated based on the proposed method. The experiment results showed that our method excels in correcting exterior and interior orientation errors, ensuring a globally optimized calibration and yielding superior results in band registration accuracy. The remainder of this paper is organized as follows: Section 2 details the proposed calibration method. Section 3 introduces the IRS of HJ-2A/B and experimental data. Section 4 presents and discusses the results. Section 5 draws the conclusion.

2. Methodology

The core idea of the proposed method is to set one master band for each FPA. The focal lengths of different FPAs and the IOPs of the master bands are solved uniformly in the bundle adjustment, achieving a global optimal result. After obtaining global optimal EOPs, the slave bands on each FPA are calibrated based on the corresponding master band. The overall technical process is shown in Figure 1. It can be decomposed into two key modules: 1) master bands calibration, and 2) slave bands calibration.

2.1 Geometric Model

2.1.1 Geometric Model of Whisk-broom Sensor
For the dynamic whisk-broom sensor, the geometric model can be expressed as follows:

$$\begin{bmatrix} X \\ Y \\ Z \end{bmatrix} = \begin{bmatrix} X_S \\ Y_S \\ Z_S \end{bmatrix} + \lambda R_{ECI}^{ECEF} R_{body}^{ECI} R_{cam}^{body} R_U R_S \begin{bmatrix} x - x_0 \\ y - y_0 \\ f \end{bmatrix} \quad (1)$$

where $[X \quad Y \quad Z]^T$ is the coordinate of a ground point in the earth-centered earth-fixed (ECEF) coordinate system; $[X_S \quad Y_S \quad Z_S]^T$ is the position of the satellite determined by the global positioning system (GPS); R_{ECI}^{ECEF} is the rotation matrix between the earth-centered inertial (ECI) coordinate system and the ECEF coordinate system; R_{body}^{ECI} is the rotation matrix between the satellite body coordinate system and the ECI coordinate system; R_{cam}^{body} is the rotation matrix of sensor installation angle in the body coordinate system; R_U is the offset matrix, which is be used to eliminate particular equipment installation and attitude errors; R_S is the rotation matrix composed of the steering mirror angle around the X axis of the sensor coordinate system during imaging; (x, y) is the coordinate of a pixel in the focal plane; (x_0, y_0) is the coordinate of the principal point; f is the focal length; λ is the scale factor.

2.1.2 Master Bands Calibration
The master bands calibration addresses three main issues: i) obtaining the distortion parameters of each master band, ii) correcting the focal length and coordinate of principal point of each FPA, and iii) obtaining the accurate EOPs of each image frame. Generally, to obtain numerous GCPs for calibration, the master band images are first matched with the reference DOMs, followed by interpolation of elevations from the reference DEMs. The matching algorithm with two steps of expansion (Zhang et al., 2016) is adopted to acquire GCPs. Since the raw master band images contain severe distortion, leading to unreliable feature point matching, image rectification is first performed based on the model in Equation (1) and the reference DEMs. Note that this matching step is only used for extracting GCPs, the subsequent bundle adjustment process is based on the coordinates of the matching points in the original images.
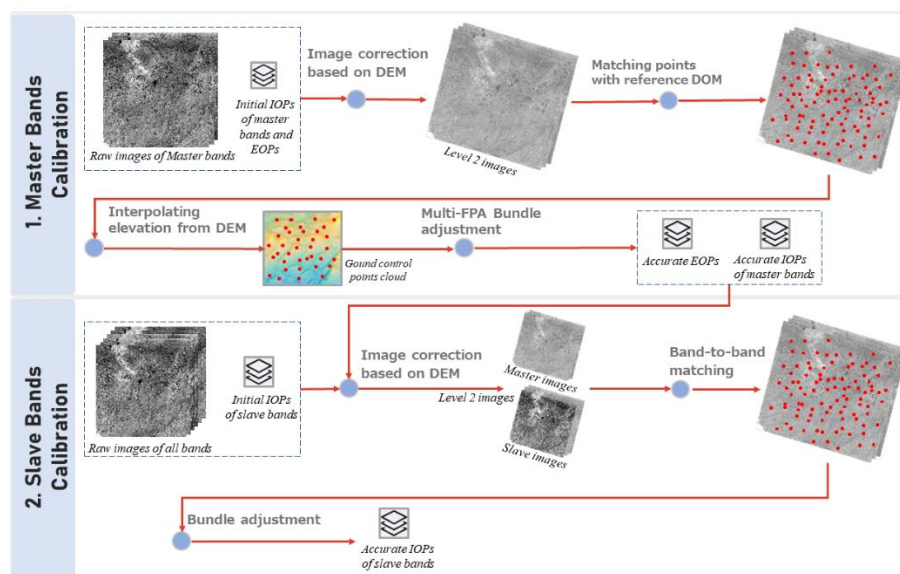

Figure 1. The workflow of the proposed calibration method.

After obtaining GCPs, multi-FPA bundle adjustment is performed. For whisk-broom sensor, the EOPs for each image frame include seven parameters: three for position, three for attitude, and one for the scanning angle. Given that solving the position and attitude for each image frame results in large parameter blocks and a time-consuming iteration process, the Lagrange Interpolation Model is employed during bundle adjustment. This model selects image frames at specific time intervals as orientation fixes. Only the EOPs of the orientation fixes are solved during bundle adjustment, and the EOPs of other image frames are interpolated based on the orientation fixes. The $3rd$-order Lagrange Interpolation Model employed in this paper can be expressed as follows:

$$P_3(t) = \sum_{i=0}^{3} P(t_i) \prod_{j=0, j\neq i}^{3} \frac{t-t_j}{t_i-t_j} \qquad (2)$$

where $P_3(t)$ at time t is interpolated from the values $P(t_i)$ at the four neighboring orientation fixes with time t_i; $P_3(t)$ is the

position and attitude parameters for image frame at time t.

The measurement of scanning angle suffers errors from variation of rotation velocity of the steering mirror, which makes the angle not be linearly correlated with time t, it can be modeled on the basis of Fourier series:

$$\theta(t) = a_0 + \sum_{i=1}^{n}[a_i \cos(i\omega t) + b_i \sin(i\omega t)] \qquad (3)$$

where $\theta(t)$ at time t is the scanning angle; $a_0, a_1, \dots, a_n, b_1, \dots, b_n$ are the coefficients of Fourier series; ω is the angular frequency; n is the order of the Fourier series, which is 8 in this paper.

After the satellite is launched, the laboratory IOPs may change due to variation in the thermal environment and physical stress release, and the effective focal length differs for each FPA. Thus, the following additional parameters model is established as

$$\begin{cases} \Delta x_i = \Delta x_{0,i} - \frac{\Delta f_i}{f}\bar{x}_i + \left(k_{1,i}r_i^2 + k_{2,i}r_i^4\right)\bar{x}_i + p_{1,i}\left(r_i^2 + 2\bar{x}_i^2\right) + 2p_{2,i}\bar{x}_i\bar{y}_i \\ \Delta y_i = \Delta y_{0,i} - \frac{\Delta f_i}{f}\bar{y}_i + \left(k_{1,i}r_i^2 + k_{2,i}r_i^4\right)\bar{y}_i + 2p_{1,i}\bar{x}_i\bar{y}_i + p_{2,i}\left(r_i^2 + 2\bar{y}_i^2\right) \end{cases} \qquad (4)$$

where i is the index of each FPA; $(\Delta x_{0,i}, \Delta y_{0,i})$ is the correction term of principal point coordinate; $k_{1,i}$, $k_{2,i}$ are the radial distortion parameters; $p_{1,i}$, $p_{2,i}$ are the decentering distortion parameters; $(\bar{x}_i, \bar{y}_i) = (x - x_{0,i}, y - y_{0,i})$ and $r_i = \sqrt{\bar{x}_i^2 + \bar{y}_i^2}$; Δf_i is the correction term for each FPA.

Combining Equation (1) to (4), the master bands calibration model is as follows:

$$V_M = AX + BX_M + CX_i - L_M \qquad P_M \qquad (5)$$

where X is the vector of the corrections in the exterior orientation elements of the orientation fixes; X_M is the vector of corrections in the Fourier series parameters; X_i is the vector of corrections in the additional parameters of master band sensor arrays and focal length of each FPA; (A, B, C) are the corresponding design matrices; L_M is the corresponding

discrepancy vector; P_M is the weight matric.

2.2 Slave Bands Calibration

At the beginning of slave bands calibration, images from both master and slave bands are rectified based on the multi-FPA bundle adjustment results. Note that the geolocation accuracy of master bands images should be comparable with the reference DOMs after this rectification step. Then the slave band images are matched with the master band images that share the same FPA to get reliable feature points. Digital GCPs are obtained by interpolating the elevation of matching points from reference DEMs.

Based on the accurate EOPs, and the corresponding focal lengths and coordinates of principal points, the slave bands calibration focuses solely on adjusting the sensor array offset and distortion parameters, expressed as

$$\begin{cases} \Delta x_j = \Delta x_j + \left(k_{1,j}r_j^2 + k_{2,j}r_j^4\right)\bar{x}_j + p_{1,j}\left(r_j^2 + 2\bar{x}_j^2\right) + 2p_{2,j}\bar{x}_j\bar{y}_j \\ \Delta y_j = \Delta y_j + \left(k_{1,j}r_j^2 + k_{2,j}r_j^4\right)\bar{y}_j + 2p_{1,j}\bar{x}_j\bar{y}_j + p_{2,j}\left(r_j^2 + 2\bar{y}_j^2\right) \end{cases} \qquad (6)$$

Equation (6) is performed based on Equations (1) and (4), which means only the additional parameters of slave band sensor arrays are solved during the bundle adjustment. The slave bands calibration model is as follows:

$$V_S = DX_s - L_s \qquad P_s \qquad (7)$$

where X_S is the vector of corrections in the additional parameters of slave band sensor arrays; D is the corresponding design matric; L_S is the corresponding discrepancy vector; P_S is the weight matric.

3. Materials

3.1 Design of Infrared Sensor on HJ-2 A/B

Launched on September 27, 2020, HJ-2 A/B are two satellites sharing the same design. Each satellite is equipped with four types of optical payloads, including the IRS, the 16m-resolution charge-coupled device (CCD) camera, the hyperspectral imager, and the polarized scanning atmospheric corrector. Among these

instruments, the IRS has nine spectral bands covering the visible-near infrared (VNIR), short-wave infrared (SWIR), middle-wave infrared (MWIR) and long-wave infrared (LWIR), which correspond to B1 to B3 (0.63-0.69 μm, 0.73-0.77 μm, 0.78-0.9 μm), B4 to B6 (1.19-1.29 μm, 1.55-1.68 μm, 2.08-2.35 μm), B7 (3.5-4.8 μm) and B8 to B9 (10.5-11.4 μm, 11.5-12.5 μm), respectively. Arrays of B1 to B5 and B6 to B9 consist of 800 and 400 pixels respectively. The spatial resolutions of B1 to B5 are 48 m, which are twice as high as those of B6 to B9. In this paper, B1 to B2, B5 and B7 to B9 are calibrated based on B3, B4 and B6, respectively.

As shown in Figure 2 (a), the IRS collects data in one scanning direction, utilizing a steering mirror and an off-axis three-reflector optical system (OTOS) to correct image rotation. This setup achieves a large scanning angle of 60° and a wide swath of 720 km. The collected radiation is projected onto three FPAs. For B4 and B5, the radiation is reflected six times—once more than for the other bands—resulting in inverted images compared to those of the other bands. One scanning cycle of the IRS is about 5.331 s, including 4 s for imaging and 1.331 s for returning

the steering mirror. The imaging commences only when the steering mirror moves at a uniform speed. To mitigate satellite jitter, an angular momentum elimination device is used to suppress rotational inertia as the steering mirror returns.
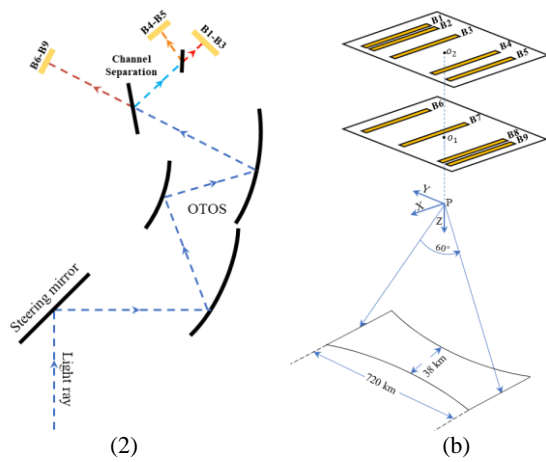

Figure 2. Mechanism design of the IRS of HJ-2 A/B(a) and the equivalent imaging sketch (b).

The equivalent camera model, as shown in Figure 2 (b), reveals that all detector linear arrays are arranged off-principal-point.

This arrangement means detectors across different bands observe the same ground object at varying times. It is designed that the focal lengths of B1 to B5 and B6 to B9 are about 337.7 and 268.6 mm, respectively. However, focal lengths of B1 to B3 are not the same as those of B4 to B5 since these two groups of arrays are arranged on different assemblies.

3.2 Dataset

Considering that HJ-2 B shares the same type payloads and calibration procedure with HJ-2 A, the experiment exclusively utilizes images from the IRS of HJ-2 A. Figure 3 displays the coverage and overview of the three experimental images, denoted as A, B, and C. To achieve a satisfactory matching result, these images were carefully selected with little cloud cover. Dataset A was used for calibration, while datasets B and C were prepared for comparison with different calibration methods in terms of georeferencing accuracy and band registration accuracy. Datasets A, B, and C were collected on January 19, February 18, and January 17, 2021, covering areas of 536,289 sq km, 536,414 sq km, and 595,431 sq km, respectively.

The IRS collects data for about ten minutes each time it is turned on, which means there are about 118 whisk-broom images in each imaging mission. To facilitate image processing, these whisk-broom images are divided according to the coverage area. Respectively, there are 19, 19 and 21 whisk-broom images in datasets A, B, and C.
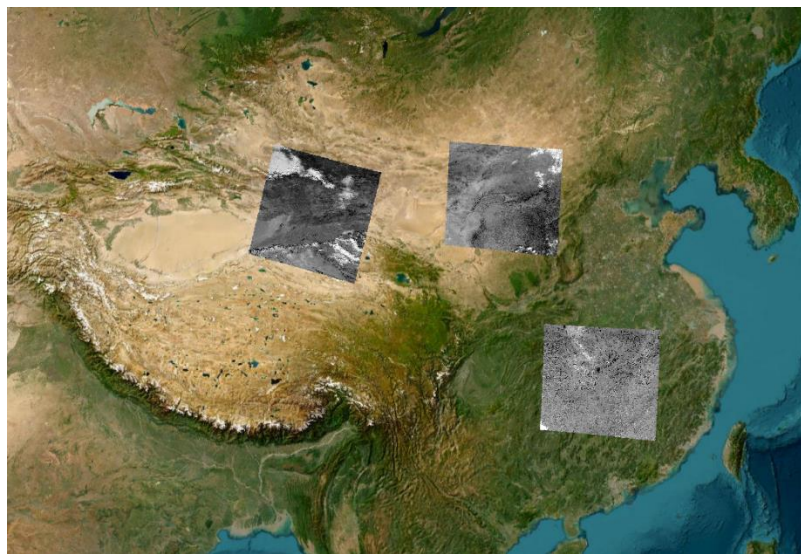

Figure 3. Coverage and the IRS images of B3 of study area.

To support the calibration work, the 15 m DOM from Landsat images and the global 30 m Shuttle Radar Topography Mission (SRTM) DEM are used as reference data.

4. Experiments and discussions

4.1 Comparative Methods and Evaluation Metrics

To assess the performance of the proposed calibration method, we chose the single master band calibration method (classical method) for comparison, which calibrated all the slave bands of different FPAs based on the bundle adjustment result of one master band. Specifically, B3 has been as the master band, with the remaining bands being calibrated were as slave bands. This approach compensated for band registration errors resulting from focal length differences by correcting x_0 and y_0.

To quantitatively evaluate the calibration performances of the two methods, two metrics have been adopted to measure the georeferencing and band registration accuracies. The performances were compared based on the evaluation dataset, indicating that the georeferencing and band registration accuracies were calculated based on the EOPs bundle adjustment using the calibration result. The two metrics are defined as follows:

- **Georeferencing accuracy.** This metric indicates the georeferencing accuracy of the master band images after calibration. Specifically, the master band images are rectified and matched with the reference DOM to obtain dense GCPs. The RMSE of the reprojection errors in the image space of the GCPs, denoted as σ^g (σ^g_{sample} and

σ_{line}^{g} are the components of σ in the sample and line directions, respectively), is calculated for quantitative evaluation of the georeferencing accuracy.

- **Band registration accuracy.** This metric indicates the band registration accuracy between the master band and slave bands after calibration. Specifically, the slave band images are matched with the corresponding master band images after rectification to obtain dense feature points. Based on the reference DEMs, the RMSE of the reprojection errors in the image space of the matching points is calculated for quantitative evaluation of the band registration accuracy.

4.2 Overall Results and Comparison

4.2.1 Quantitative Evaluation

The georeferencing accuracy and band registration accuracy are delineated in Tables 1 and 2, respectively. It is important to note that the sample direction aligns with the track, whereas the line direction traverses across the track. For datasets B and C, reference data was additionally utilized to refine the EOPs. This strategic refinement was instrumental in enhancing the evaluation of the precision achieved by the two calibration methods and in mitigating the impact arising from variations in scan angle errors among different datasets. Furthermore, as indicated in Table 2, bands 1, 2, 4, 5, and 6 were assessed for registration accuracy using band 3 as the baseline, while bands 7, 8, and 9 were evaluated in comparison to band 6. This approach was adopted due to the close wavelength similarity between bands 6 and 3, which results in a more consistent representation of surface textures in the images, thereby yielding higher matching accuracy. In contrast, the considerable wavelength disparity between bands 7, 8, 9, and band 3 heightens the risk of mismatches.

Method	Dataset	B3			B4			B6		
		σ_{sample}^{g}	σ_{line}^{g}	σ^{g}	σ_{sample}^{g}	σ_{line}^{g}	σ^{g}	σ_{sample}^{g}	σ_{line}^{g}	σ^{g}
Classical method	A	0.254	0.323	0.411	0.299	0.359	0.467	0.153	0.174	0.232
	B	0.225	0.192	0.296	0.276	0.865	0.908	0.176	0.447	0.480
	C	0.256	0.197	0.323	0.241	0.791	0.827	0.115	0.444	0.458
The proposed method	A	0.271	0.316	0.416	0.273	0.321	0.422	0.144	0.171	0.223
	B	**0.149**	0.198	0.248	0.228	**0.214**	**0.313**	0.155	**0.156**	**0.220**
	C	0.218	0.190	0.289	0.234	**0.207**	**0.312**	0.095	**0.117**	**0.151**

Table 1. Comparison of georeferencing accuracies of representative bands on each FPA (unit: pixel).

Method	Dataset	Direction	B1	B2	B4	B5	B6	B7	B8	B9
Classical method	B	Sample	0.09	0.08	0.16	0.21	0.11	0.30	0.41	0.41
		Line	0.30	0.39	0.42	0.55	0.45	0.21	0.26	0.26
		Planimetry	0.32	0.39	0.45	0.59	0.47	0.37	0.48	0.49
	C	Sample	0.10	0.10	0.10	0.15	0.14	0.15	0.19	0.21
		Line	0.32	0.42	0.40	0.55	0.47	0.29	0.34	0.36
		Planimetry	0.34	0.43	0.42	0.57	0.49	0.33	0.38	0.41
The proposed method	B	Sample	0.10	0.10	0.09	0.10	0.09	0.28	0.26	0.24
		Line	**0.16**	**0.07**	**0.13**	**0.17**	**0.15**	0.21	0.23	0.27
		Planimetry	**0.19**	**0.12**	**0.15**	**0.19**	**0.18**	0.35	0.35	0.36
	C	Sample	0.11	0.16	0.21	0.23	0.16	0.12	0.19	0.23
		Line	0.31	0.30	0.27	0.40	**0.26**	0.23	0.25	0.30
		Planimetry	0.33	0.34	0.34	0.46	**0.31**	0.25	0.31	0.38

Table 2. Comparison of band registration accuracies using B3 and B6 as reference bands (unit: pixel).

Table 1 offers a detailed comparison of our method against the baseline method when applied to calibration dataset A. Our method demonstrates a planimetric precision of 0.416 pixels in band 3, closely aligning with the baseline with a minor difference of 0.005 pixels. For bands 4 and 6, our method records precisions of 0.422 and 0.223 pixels, respectively, representing slight improvements over the baseline method. This comparison illustrates the comparable efficiency of both techniques in precision measurement, with our method showing slight enhancements in certain bands.

Regarding test datasets B and C, both our method and the baseline method used band 3 as the reference for refining EOPs. This resulted in similar geometric positioning accuracies in band 3 across both methods. However, our method achieved planimetric accuracies of 0.248 pixels for dataset B and 0.289 pixels for dataset C, demonstrating consistent improvements in precision. Significantly, in bands 4 and 6, our method exhibited considerable precision advantages, with accuracies substantially exceeding those of the baseline method. These results underscore the robustness of our calibration process, particularly in line direction calibration and scan direction, as evidenced in bands 4 and 6.

Moreover, the distinct advantage of our method is further underscored by the results for datasets B and C, as detailed in Table 2. In this case, our method's planimetric registration accuracy clearly outperforms the baseline. For instance, in dataset B, the accuracy for band 5 reached 0.19 pixels with our method, significantly better than the baseline's 0.59 pixels. Similarly, in dataset C, our accuracy for band 1 was 0.33 pixels, slightly exceeding the baseline's 0.34 pixels. This comparative analysis between datasets B and C emphasizes our method's enhanced effectiveness, especially with dataset B, where differences in platform attitude and scan mirror angle errors during data acquisition were more pronounced.

Importantly, a 5*th*-order Fourier series correction was applied to

both datasets. However, the effectiveness of the correction varied, being less so for dataset C. This underlines the impact of scan angle correction precision on registration accuracy among different bands. While a higher order Fourier series could potentially improve results for dataset C, it also carries the risks of overfitting and increased computational demands. The baseline method's consistent planimetric registration accuracy across datasets B and C suggests inherent calibration limitations, particularly in optimizing the primary band, leading to a compromised correction outcome in other bands. This disparity accentuates the global optimization capability of our method in

achieving refined intrinsic parameters.

4.2.2 Error Distribution of GCPs

In the interest of advancing the analytical discourse, Figure 4 and 5 have been prepared to illustrate the reprojection errors in the control points for bands 3, 4, and 6, both pre- and post-calibration. This delineation facilitates a deeper understanding of the calibration impact. Specifically, the intrinsic calibration of bands 1 and 2 referenced the metrics of band 3. Similarly, band 5's calibration was predicated on the parameters of band 4, while bands 7, 8, and 9 were calibrated in alignment with the characteristics of band 6.
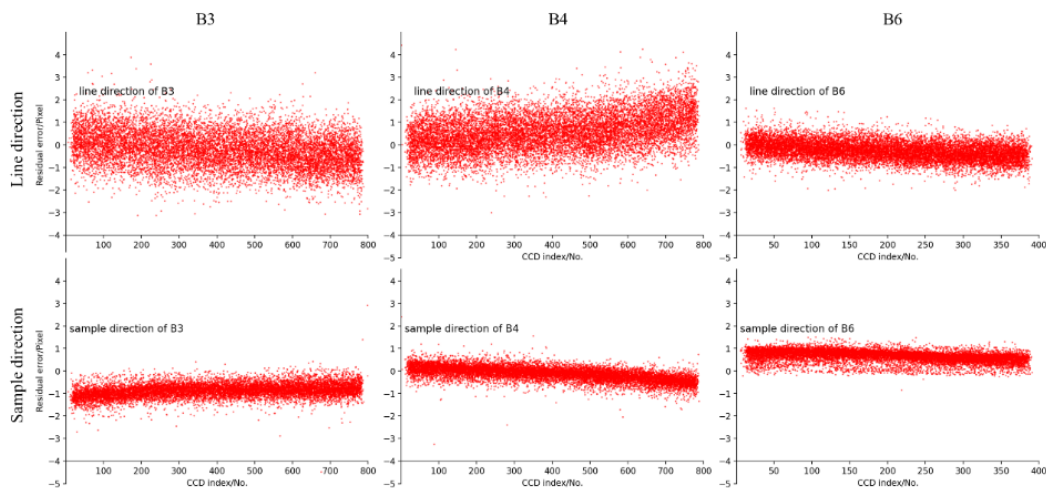

Figure 4. Reprojection Errors of Control Points for Bands 3, 4, and 6 Along Sample and Line Directions Before Calibration.
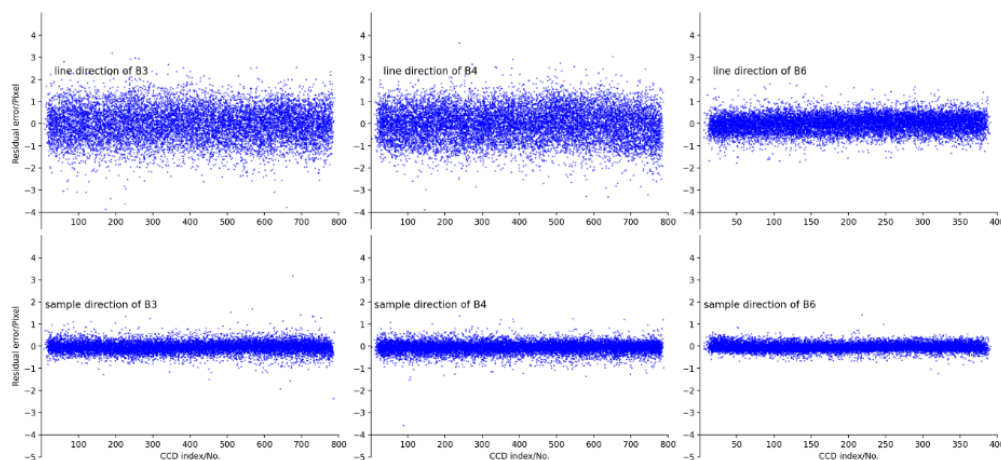

Figure 5. Reprojection Errors of Control Points for Bands 3, 4, and 6 Along Sample and Line Directions After Calibration.

Comparing Figure 4 and 5 reveals that bands 3, 4, and 6 exhibit pronounced distortion patterns prior to calibration. The error curves of these bands show distinct trends, indicating that errors in the principal point offset and focal length predominantly affect the curves deviation in both the sample and line directions. Meanwhile, the lens distortion parameters affect the slope or polynomial order of these curves. Therefore, Figure 4 underscores the necessity of setting distinct calibration parameters for different FPAs. Additionally, the error distribution in the line direction is not as concentrated as in the sample direction, due to alignment with the scanning mirror's sweep. The non-ideal and non-uniform motion of the scanning mirror impacts the error distribution in the line direction.

The error curves in Figure 5 clearly show the elimination of the distortion patterns in both line and sample directions is apparent, underscoring the effectiveness of our method in compensating for the interior orientation errors in bands 3, 4, and 6. Our approach has produced globally optimal results for these bands, thereby enhancing their geometric precision and ensuring accurate band registration.

5. Conclusion

This study presents a multi-focal-plane-array joint calibration method for the HJ-2 A/B satellite's whisk-broom sensors, marking a significant advancement in the field of the infrared remote sensing calibration. By integrating master bands and

applying comprehensive bundle adjustments, we achieved notable improvements in georeferencing and multispectral band registration accuracy, surpassing traditional method. This method effectively addresses the dual challenges of exterior and interior orientation accuracy, offering a comprehensive solution to the unique calibration requirements of whisk-broom sensors. The resulting enhancements in object localization, area estimation, and terrain analysis highlight the importance of the holistic calibration approach.

References

Cao, H., Tao, P., Li, H., Shi, J., 2019. Bundle adjustment of satellite images based on an equivalent geometric sensor model with digital elevation model. *ISPRS Journal of Photogrammetry and Remote Sensing*, 156, 169–183.

Caporali, A., Zurutuza, J., 2021. Broadcast ephemeris with centimetric accuracy: test results for GPS, Galileo, Beidou and GLONOSS. *Remote Sensing*, 13(20), 4185.

Corsi, C., 2010. History highlights and future trends of infrared sensors. *Journal of Modern Optics*, 57(18), 1663–1686.

Fang, Z., Wang, X., Ji, W., Xu, M., Zhang, Y., Li, Y., Li, L., 2021. Geometric Calibration and Image Quality Assessment of High Resolution Dual-Camera Satellite. *Journal of Beijing Institute of Technology*, 30(2), 125–138.

Fowler, J. E., 2014. Compressive pushbroom and whiskbroom sensing for hyperspectral remote-sensing imaging. *2014 IEEE International Conference on Image Processing (ICIP)*, IEEE, 684–688.

Garcia, M., Oliveira, H., 2020. The Influence of Ground Control Points Configuration and Camera Calibration for DTM and Orthomosaic Generation Using Imagery Obtained from a Low-Cost UAV. *ISPRS Annals of the Photogrammetry, Remote Sensing and Spatial Information Sciences*, 1, 239–244.

Hugenholtz, C., Brown, O., Walker, J., Barchyn, T., Nesbit, P., Kucharczyk, M., Myshak, S., 2016. Spatial accuracy of UAV-derived orthoimagery and topography: Comparing photogrammetric models processed with direct geo-referencing and ground control points. *Geomatica*, 70(1), 21–30.

Li, J., 2021. Satellite Remote Sensing Technologies. Springer.

Liu, T., Burner, A. W., Jones, T. W., Barrows, D. A., 2012. Photogrammetric techniques for aerospace applications. *Progress in Aerospace Sciences*, 54, 1–58.

Liu, Y., Qian, J., Yue, H., 2021. Comprehensive evaluation of Sentinel-2 red edge and shortwave-infrared bands to estimate soil moisture. IEEE *Journal of Selected Topics in Applied Earth Observations and Remote Sensing*, 14, 7448–7465.

Pan, H., Cui, Z., Hu, X., Zhu, X., 2022a. Systematic geolocation errors of FengYun-3D MERSI-II. *IEEE Transactions on Geoscience and Remote Sensing*, 60, 1–11.

Pan, H., Tian, J., Wang, T., Wang, J., Liu, C., Yang, L., 2022b. Band-to-Band Registration of FY-1C/D Visible-IR Scanning Radiometer High-Resolution Picture Transmission Data. *Remote Sensing*, 14(2), 411.

Schorlemer, J., Schulz, C., Pohl, N., Rolfes, I., Barowski, J., 2021. Compensation of sensor movements in short-range FMCW synthetic aperture radar algorithms. *IEEE Transactions on Microwave Theory and Techniques*, 69(11), 5145–5159.

Sheng, Q., Wang, Q., Xiao, H., Wang, Q., 2018. Research on geometric calibration of spaceborne linear array whiskbroom camera. *Sensors*, 18(1), 247.

Tao, P., Lu, L., Zhang, Y., Xu, B., Zou, S., 2014. On-orbit geometric calibration of the panchromatic/multispectral camera of the ZY-1 02C satellite based on public geographic data. *Photogrammetric Engineering & Remote Sensing*, 80(6), 505–517.

Tilton, J. C., Wolfe, R. E., Lin, G., Dellomo, J. J., 2019. On-orbit measurement of the effective focal length and Band-to-Band registration of satellite-borne whiskbroom imaging sensors. *IEEE Journal of Selected Topics in Applied Earth Observations and Remote Sensing*, 12(11), 4622–4633.

Tong, X., Liu, X., Chen, P., Liu, S., Luan, K., Li, L., Liu, S., Liu, X., Xie, H., Jin, Y. et al., 2015. Integration of UAV-based photogrammetry and terrestrial laser scanning for the three-dimensional mapping and monitoring of open-pit mine areas. *Remote Sensing*, 7(6), 6635–6662.

Toutin, T., 2004. Geometric processing of remote sensing images: models, algorithms and methods. *International Journal of Remote Sensing*, 25(10), 1893–1924.

Ye, J., Lin, X., Xu, T., 2017. Mathematical modeling and accuracy testing of worldview-2 level-1B stereo pairs without ground control points. *Remote Sensing*, 9(7), 737.

Zhang, Y., Zheng, M., Xiong, J., Lu, Y., Xiong, X., 2013. On-orbit geometric calibration of ZY-3 three-line array imagery with multistrip data sets. *IEEE Transactions on Geoscience and Remote Sensing*, 52(1), 224–234.

Zhang, Z., He, J., Huang, S., Duan, Y., 2016. Dense image matching with two steps of expansion. *The International Archives of the Photogrammetry, Remote Sensing and Spatial Information Sciences*, 41, 143–149.